



Analysis of the performances of a marine propeller operating in oblique flow



Giulio Dubbioso ^{a,*}, Roberto Muscari ^a, Andrea Di Mascio ^b

^a Istituto Nazionale per Studi ed Esperienze di Architettura Navale (CNR-INSEAN), Via di Vallerano 139, 00128 Roma, Italy

^b Istituto per le applicazioni del calcolo "Mauro Picone" (CNR-IAC), via dei Taurini 19, 00185 Roma, Italy

ARTICLE INFO

Article history:

Received 22 October 2012

Received in revised form 17 December 2012

Accepted 15 January 2013

Available online 8 February 2013

ABSTRACT

The present work is aimed to assess the capability of a numerical code based on the solution of the Reynolds averaged Navier–Stokes equations for the study of propeller functioning in off design conditions; this aspect is becoming of central interest in naval hydrodynamics research because of its crucial implications on design aspects and performance analysis of the vessel during its operational life. A marine propeller working in oblique flow conditions is numerically simulated by the unsteady Reynolds averaged Navier–Stokes equations (uRaNSe) and a dynamically overlapping grid approach. The test case considered is the CNR-INSEAN E779A propeller model. Two different loading conditions have been analyzed at different incidence angles (10–30°) in order to characterize the propeller performance during idealized off-design conditions, similar to those experienced during a tight manoeuvre. The main focus is on hydrodynamic loads (forces and moments) that act on a single blade, on the hub and on the complete propeller; peculiar characteristics of pressure distribution on the blade and downstream wake will be presented as well. Verification of the numerical computations have been assessed by grid convergence analysis.

© 2013 Elsevier Ltd. All rights reserved.

1. Introduction

Propeller performance prediction has been traditionally centered on ship's design requirements in straight ahead sailing, focusing mainly, in case of standard propulsion configurations (single or multi-screw), on thrust and torque hydro-loads. Strictly speaking, a screw propeller is designed in order to satisfy a prescribed requirement (maximization of the overall propulsive efficiency and/or minimization of the cavitation phenomena) by a suitable adaptation of the incidence of the blade sections to the ship wake experienced at the required speed. However, during its operational life, a vessel may experience different off-design scenarios, like maneuvering and crash stop, which change completely the working regime of the propeller. In these cases, in fact, propeller loads can increase abruptly with respect to those experienced during the straight ahead motion, because of complex flow field phenomena and interactions between hull, propeller and rudder; moreover, in these circumstances, additional forces and moments are generated (or at least, amplified) in the propeller plane which may affect profoundly the dynamic response of the vehicle. A deep analysis of full scale sea trial tests for a broad set of twin screw naval vessel reported in [1] showed that, during turning circle manoeuvres, propeller power/torque demand increase up to 100% and 50% of the value in the approach phase (straight path)

for the external (relatively to the center of the turn) and internal propellers, respectively. Quantification of the asymmetrical distribution of loads is essential in order to develop suitable control system strategies for preventing excessive structural loads [2], while not reducing the operational capabilities of the vessel. Numerical simulations [3] focused on the steady turning phase of a twin screw naval vessel revealed that, during the steady turn, the hull wake is asymmetric with predominant large vortical structures caused both by massive separation phenomena due to the cross-flow velocity on the internal side, and by a relevant lateral speed component (up to 30°) due to the combined sway-yaw motion. It is evident, therefore, that the propeller works in a wake envelope markedly different from the one met during straight ahead operation. In-plane loads exerted by the propeller blades during drift motion can affect profoundly the dynamic response (course stability and turning qualities) of the vessel, also. Despite the contribution of the propeller to the dynamic stability of airplanes has been investigated since the Second World War [4], its influence on ship's maneuvering behavior has been first assessed recently in [5] by means of circular motion tests on the DDG51 destroyer model. Numerical computations performed on a twin screw single rudder tanker like vessel [6,7], stressed that usual actuator disk model (broadly adopted for simulation of self propulsion tests) do not account for a lateral force. An hybrid model consisting in the actuator disk for treating the axial component of the flow and the Ribner lateral force model for the modeling of oblique effects have been proposed with promising results. Moreover, similar computations,

* Corresponding author. Tel.: +39 3492942426.

E-mail address: giudubbioso@libero.it (G. Dubbioso).

carried out on the same vessel equipped with a different configuration, further stressed the need for a propeller lateral force model for estimating complex phenomena related to rudder-propeller interaction [8]. During crash stop manoeuvres, huge loads are generated by the propeller blades and exerted to the propulsion device elements (shaft line, brackets and pitch control mechanism) as well as to the hull structures. In particular, it has been observed that, during the last phase of the deceleration, i.e. during the “axial jet” state [9], a relevant side force arises, imparting an unpredictable yawing-drift motion to the vessel. In turn, this motion may increase the risk of collision with obstacles or other vessels, and, secondarily, will induce an additional oblique flow component which may amplify unsteady loads, further stressing the propulsion device.

On the basis of the above considerations, investigation of the propeller functioning in off-design condition is of paramount importance in order to improve the propulsion system sizing and design. Moreover, relevant loads exerted by the propeller during manoeuvres should be reliably predicted in order to provide an accurate estimation of the vessel dynamic response. Traditional numerical approaches like BEM (Boundary Element Method) or VLM (Vortex Lattice Method) accurately predict the hydrodynamic characteristics of the propeller in typical design conditions, namely in open water or in a wake field typical of a ship advancing straight on its path or, in general, when the cross-flow components are negligible with respect to the axial one. Accuracy of these approaches for typical propeller off-design operations may be spoiled by massive unsteady separation and/or cavitation phenomena which are intrinsically not accounted for in these formulations. On the other hand, Computational Fluid Dynamics (CFD) approaches based on the direct solution of the Navier–Stokes equations can be an attractive alternative because of their ability to treat viscous effects and separation phenomena; moreover, in addition to the global loads generated on the propeller blades and hub, details of the flow field surrounding the propeller and, in particular, the evolution of the convected wake can be investigated in details.

In the present work the performance of a rotating propeller set at incidence with respect to the inflow is investigated by means of an approach based on the numerical solution of the unsteady Reynolds averaged Navier–Stokes equations (uRaNSe). The selected propeller is the four bladed INSEAN E779A model, for which high quality data for CFD validation exist [10,11]. The hydrodynamic solver is the in-house code χ_{navis} , which is a finite volume uRaNSe solver. The rotation of the propeller with respect to the fixed background is handled by a dynamic overset grids technique.

The principal aim of the present work is to contribute to the understanding of propeller behavior during off-design conditions, with particular focus on the in-plane loads acting on the propeller hub and, consequently transmitted to the vessel during its motion. Moreover, the results achieved by simulating the rotating propeller in behind hull condition [12,13] may provide an exhaustive overview of the flow field in the hull stern region, as well as very promising results in terms hydrodynamic loads on the hull and appendages [14,15] and kinematic properties of the vessel under rudder action. Unfortunately, prohibitive computational time and memory resource make this choice unpractical for routine tasks. Instead of directly solving the rotating propeller, simplified models able to mimic the peculiar physic of the propeller in fully unsteady conditions and, at the same time, computationally efficient, are the most attractive approach in ship maneuvering research. In [7] two different propeller models have been considered, namely a Blade Element model and the hybrid one previously introduced [16], in order to solve the gap of the actuator disk model to model reliably oblique flow effects. Despite their computational efficiency, both BEMT and Ribner models rely on semi-empirical coefficients that should be properly tuned. The present computations, covering a

relatively broad range of propeller working conditions, may contribute to gain more insight into the sensitivity of the models to the variation of these constant, and, moreover, provide a valuable aid to the tuning process.

2. Mathematical model

The flow generated by a solid body moving in a fluid can be modeled by the unsteady Reynolds averaged Navier–Stokes equations. Within the assumption of an incompressible fluid, the set of equations is written in non-dimensional integral form with respect to a moving control volume \mathcal{V} as

$$\begin{aligned} \oint_{S(\mathcal{V})} \mathbf{U} \cdot \mathbf{n} dS &= 0 \\ \frac{\partial}{\partial t} \int_{\mathcal{V}} \mathbf{U} dV + \oint_{S(\mathcal{V})} (\mathcal{F}_c - \mathcal{F}_d) \cdot \mathbf{n} dS &= 0 \end{aligned} \quad (1)$$

where $S(\mathcal{V})$ is the boundary of the control volume, and \mathbf{n} the outward unit normal; the equations are made non-dimensional by a reference velocity (typically the free stream velocity U_∞) and a reference length L and the water density ρ . In Eq. (1), \mathcal{F}_c and \mathcal{F}_d represent Eulerian (advection and pressure) and diffusive fluxes, respectively:

$$\begin{aligned} \mathcal{F}_c &= p\mathbf{I} + (\mathbf{U} - \mathbf{V})\mathbf{U} \\ \mathcal{F}_d &= \left(\frac{1}{Rn} + v_t \right) [\text{grad}\mathbf{U} + (\text{grad}\mathbf{U})^\top] \end{aligned} \quad (2)$$

where $\mathbf{U} = (u, v, w)$ is the fluid velocity, p is the hydrodynamic pressure and \mathbf{V} the local velocity of the boundary of the control volume. In the expression of the diffusive flux, $Rn = U_\infty L/v$ is the Reynolds number, v being the kinematic viscosity, whereas v_t denotes the non-dimensional turbulent viscosity.

3. Numerical method

The numerical solution of the governing Eqs. (1) is computed by means of the solver χ_{navis} , which is a general purpose simulation code developed at INSEAN; the code yields the numerical solution of the uRaNSe with proper boundary and initial conditions. It is formulated as a finite volume scheme, with variables co-located at cell centers. Turbulent stresses are taken into account by the Boussinesq hypothesis; several turbulence models (both algebraic and differential) are implemented. In the present computations, the one-equation model originally introduced by [17] has been used. Complex geometries and multiple bodies in relative motion are handled by a suitable dynamical overlapping grid approach; high performance computing is achieved by an efficient hybrid shared and distributed memory parallelization. In the following subsections the main features of the numerical algorithm are briefly recalled; the interested reader is referred to [18–22] for details.

3.1. Spatial discretization

For the numerical solutions of the governing Eqs. (1), the computational domain D is partitioned into N_l structured blocks D^l , each one subdivided into $N_i \times N_j \times N_k$ hexahedrons D_{ijk}^l . In the numerical scheme adopted here, the blocks are not necessarily disjoint, but can be partially overlapped, as it is explained in the following. Conservation laws are then applied to each finite volume:

$$\begin{aligned} \sum_{s=1}^6 \int_{(S_{ijk}^l)_s} \mathbf{U} \cdot \mathbf{n} dS &= 0 \\ \frac{\partial}{\partial t} \int_{V_{ijk}^l} \mathbf{U} dV + \sum_{s=1}^6 \int_{(S_{ijk}^l)_s} (\mathcal{F}_c - \mathcal{F}_d) \cdot \mathbf{n} dS &= 0 \end{aligned} \quad (3)$$

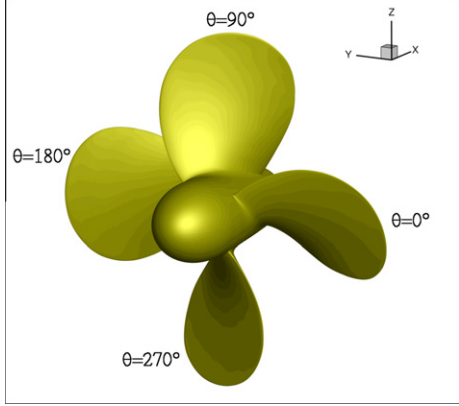


Fig. 1. Frame of reference.

Table 3
Details of grid cells distribution.

Domain	Fine	Medium	Coarse	%
4 Blades	2.36M	0.295M	0.037M	20.9
Propeller hub	0.64M	0.085M	0.011M	5.6
Near wake field (tip)	3.11M	0.388M	0.048M	27.5
Near wake field (other)	2.13M	0.266M	0.033M	18.8
Buffer zone	1.89M	0.236M	0.029M	16.7
Background	1.18M	0.148M	0.018M	10.4
Total	11.31M	1.415M	0.176M	100

In order to remove any stability constraint on the time step, an implicit scheme is considered: the time derivative in the system (4) is approximated by a second order accurate three-points backward formula

$$\Lambda \frac{3(\mathcal{V}\mathbf{q})_{ijk}^l|^{n+1} - 4(\mathcal{V}\mathbf{q})_{ijk}^l|^{n-1}}{2\Delta t} + \mathcal{R}_{ijk}^l|^{n+1} = \mathbf{0} \quad (6)$$

where the superscript n denotes the time level and Δt is the physical time step. In the solution of unsteady flows, Eq. (6) represents a system of coupled non-linear algebraic equations, that are solved iteratively by a dual time integration (see [26] for more details); to this end, a pseudo-time derivative is introduced in the discrete system of equations as

$$\tilde{\Lambda} \frac{(\mathcal{V}\mathbf{q})_{ijk}^l|^{m+1} - (\mathcal{V}\mathbf{q})_{ijk}^l|^{m-1}}{\Delta\tau} + \Lambda \frac{3(\mathcal{V}\mathbf{q})_{ijk}^l|^{m+1} - 4(\mathcal{V}\mathbf{q})_{ijk}^l|^{m-1}}{2\Delta t} + \mathcal{R}_{ijk}^l|^{m+1} = \mathbf{0} \quad (7)$$

$\Delta\tau$ being the pseudo time step, $\tilde{\Lambda} = \text{diag}(1/\beta, 1, 1, 1)$ and β the pseudo-compressibility factor [27]. Then the solution is iterated to steady state with respect to the pseudo time τ for each physical time step; the system (7) is solved by means of the approximated factorization scheme by [28]. Local dual time step and an efficient multi-grid technique are used in order to improve the convergence rate of the sub-iteration algorithm [29]. For steady problem, the solution can be achieved either as asymptotic solution of the unsteady problem or neglecting the physical time derivative in (7) and iterate in the pseudo-time only.

3.2.1. Overlapping grids approach

In this section the basic elements of the overlapping grid approach (or “Chimera” method) implemented in the solver χ_{navis} for both fixed grids and its extension to moving grids are briefly described. For more details, and examples of applications the reader is referred to [30,19,31,32]. The introduction of overlapping grid capabilities in the uRaNSe code is made through a modification of both the boundary conditions and internal point treatment for those zones where overlapping appears. In particular, on some boundaries the solution needs to be interpolated from other blocks. For each of these cell faces, a “donor” cell must be found. In order to retain the best approximation, if a boundary cell fall within more than one donor cell, the smallest one is chosen as basis for interpolation. Once the donor is identified, then a convex set of eight donor cell centers is searched, and a tri-linear interpolation is used to transfer the solution from one block to the boundary of the one under analysis.

As to internal points, possible overlapping for each cell centers are sought first. If overlapping is found, the cell is marked as a “hole” only if the donor cell is smaller than the one considered. As for boundary cell centers, if more than one possible donor is found, the smallest one is chosen. Differently from standard chimera approaches, however, the cell marked as holes are not removed from the computation but the interpolated solution is

Table 1
Geometric parameters of the propeller.

Propeller E779A	
Diameter	$D = 0.227$
Number of blades	$Z = 4$
Pitch ratio	$P/D = 1.1$
Rake	$4^\circ 35'$ (forward)
Expanded area ratio	0.689
Hub ratio	0.200

Table 2
Test cases.

$J = 0.88$	Grid		$J = 0.60$	Grid	
β°	Medium	Fine	β°	Medium	Fine
10	X	X	10	X	-
20	X	-	20	X	-
30	X	-	30	X	X

where \mathcal{V}_{ijk}^l is the measure of the finite volume D_{ijk}^l and $(S_{ijk}^l)_s$ indicates its s th face.

In order to achieve second order accuracy in space, convective and viscous fluxes in the momentum equations, as well as surface integrals of the velocity in the continuity equation, are computed by means of the midpoint rule, and therefore all the quantities are evaluated at cell faces centroids. A standard second order centered scheme is used for the computation of viscous terms, whereas high order Godunov-type schemes [23] can be applied for the computation of Eulerian terms (see [21]) i.e. a second order Essentially non-Oscillatory (ENO) scheme [24], a third order upwind [25], or a fourth order centered scheme. For the simulation reported in the following, the third order upwind scheme was always adopted.

3.2. Temporal integration and dual time stepping

The semi-discrete system of equations can be recast in vector form as:

$$\Lambda \frac{\partial \mathcal{V}\mathbf{q}}{\partial t} + \mathcal{R}_{ijk}^l = \mathbf{0} \quad (4)$$

where \mathcal{R}_{ijk}^l represents the flux balance for the finite volume D_{ijk}^l , $\Lambda = \text{diag}(0, 1, 1, 1)$ and

$$\mathbf{q} = \frac{1}{V_{ijk}^l} \int_{V_{ijk}^l} (p, u, v, w)^T dV \quad (5)$$

is the volume average of the unknowns.

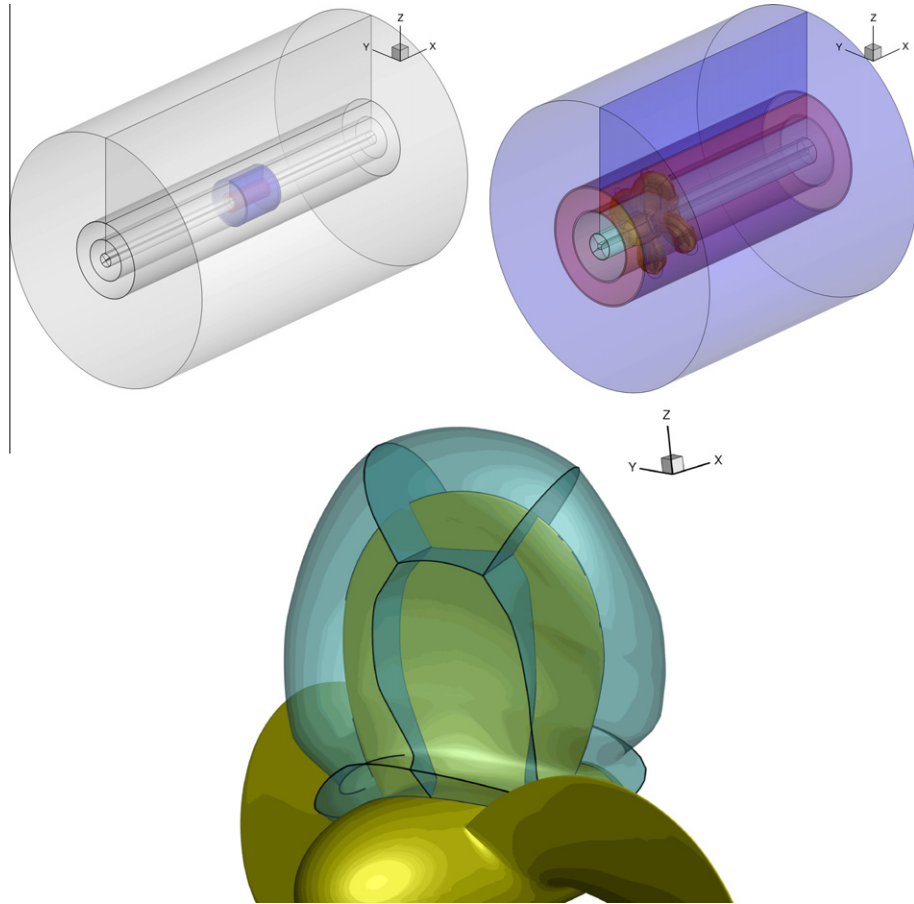


Fig. 2. Grid topology: overview (upper left), zoom of the near field (upper right) and of the blade.

enforced by adding a forcing term to the Navier–Stokes equations, in a “body-force” fashion:

$$\begin{aligned} \tilde{\lambda} \frac{(\mathcal{V}\mathbf{q})_{ijk}^l|^{m+1} - (\mathcal{V}\mathbf{q})_{ijk}^l|^m}{\Delta t} + \\ \lambda \frac{3(\mathcal{V}\mathbf{q})_{ijk}^l|^{m+1} - 4(\mathcal{V}\mathbf{q})_{ijk}^l|^n + (\mathcal{V}\mathbf{q})_{ijk}^l|^{n-1}}{2\Delta t} + \\ [\mathcal{R}_{ijk}^l|^{m+1} + \frac{k}{\delta} ((\mathcal{V}\mathbf{q})_{ijk}^l|^m - (\mathcal{V}\mathbf{q})_{\text{interp}}|^m)] = \mathbf{0} \end{aligned} \quad (8)$$

In the previous equation \mathbf{q}_{ijk}^l is the vector of the dependent variables at the cell ijk (of block l) marked as hole, \mathcal{R}_{ijk}^l is the vector of residuals, $k = \mathcal{O}(10)$ is a parameter chosen through numerical tests, and δ is the minimum between the cell non-dimensional diameter and the non-dimensional time step. This approach is particularly useful when using multigrid and approximate factorization, as it allows to maintain a structured data set. For the points that fall within a rigid body, the forcing term in the equation is analogous to the previous one, but the velocity in the forcing term is equal to the local velocity of the body.

When dealing with moving grids, grid topology must be recomputed at each time step. In order to speed-up the algorithm, a nested search technique that exploits the multigrid structure of the code is used.

3.2.2. Code parallelization

The coarse/fine grain parallelization of the unsteady uRaNSE code has been achieved by distributing the structured blocks among the available distributed (nodes) or shared memory (threads) processors, and by spreading the computational work to be done (mostly in terms of do loop inside each block among available shared memory processors). Pre-processing tools, which

allows the splitting of the structured blocks and the distribution of them among the processors, were developed for load balancing, whereas fine tuning is left to the user. Communication between processors for the coarse grain parallelization is obtained by using standard Message Passing Interface (MPI) library, whereas fine grain (shared memory) parallelization is achieved by means of the Open Message Passing (OpenMP) library. The efficiency of the parallel code has been investigated in [22] (to which the reader is referred for details), where satisfactory speed up performances have been shown in different test cases.

4. Geometry and numerical setup

The propeller selected for this study is the E779A INSEAN model, a modified Wageningen propeller characterized by a constant pitch distribution and very low skew. Views of the propeller are shown in Fig. 1 whereas the essential geometric characteristics are summarized in Table 1. In Table 2 the analyzed test cases are reported with the relative grid level refinement. The propeller has been tested for two different advance coefficients $J = U_\infty/nD$ (i.e., propeller loading), covering a relatively broad set of incidence angles (up to 30°). Numerical computations have been carried out with the medium grid for each case in the test matrix, in order to investigate and characterize the global behavior of the propeller. Furthermore, computations on the finest grid have also been performed for the two conditions that may be more representative of a real ship maneuvering scenario, namely $J = 0.88$ at 10° and $J = 0.6$ at 30°. The former case is typically met during the first instants of the manoeuvre (the propeller loading is close to the one experienced during the approach phase, and the low values

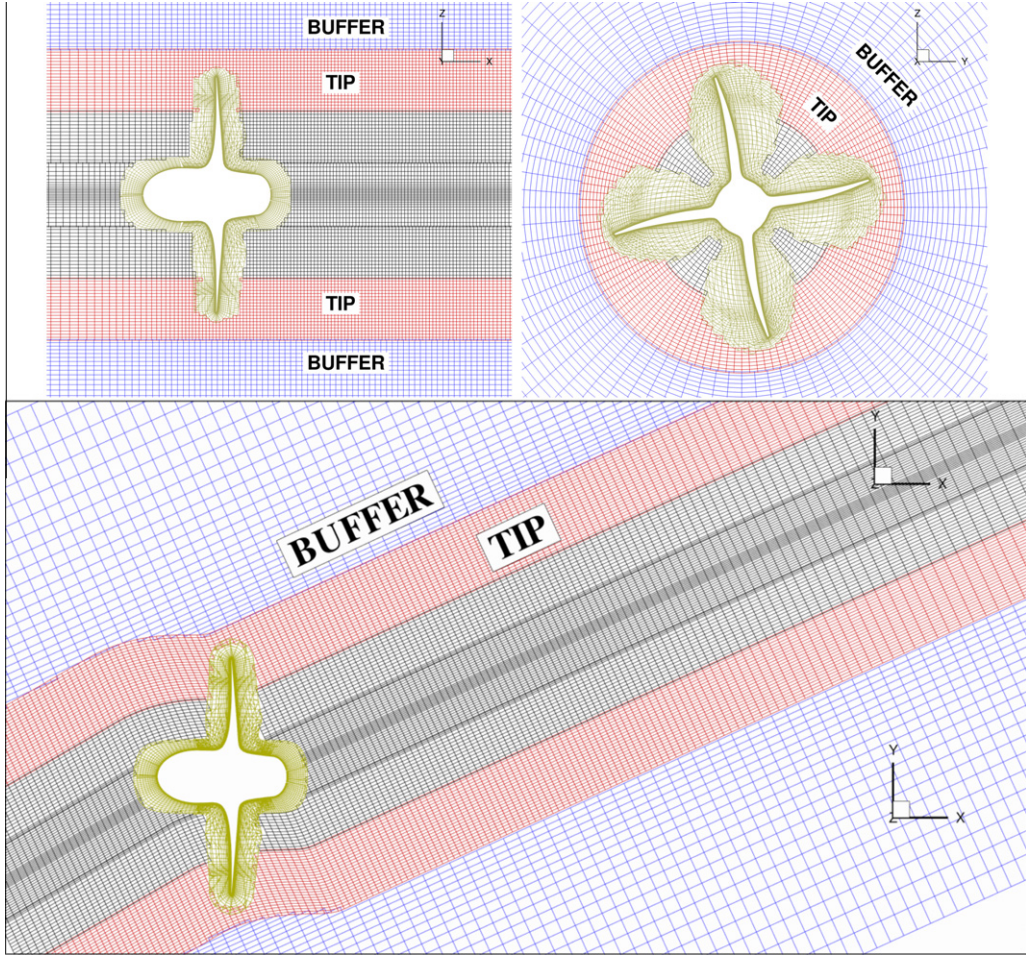


Fig. 3. Slices of the computational domain for $y = 0$ (upper left), $x = 0$ (upper right) and $z = 0$ (bottom).

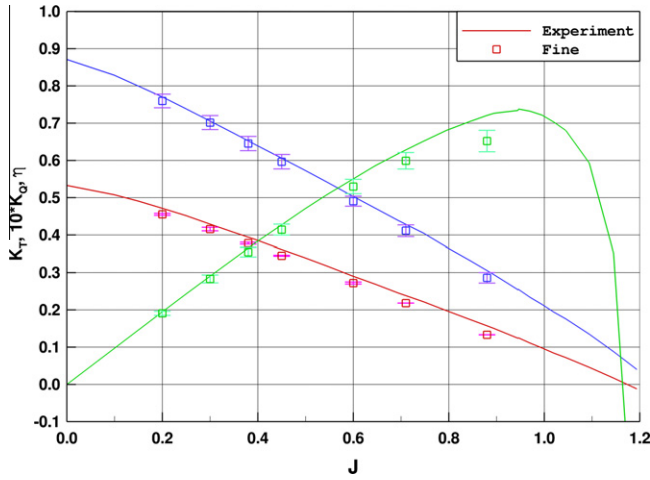


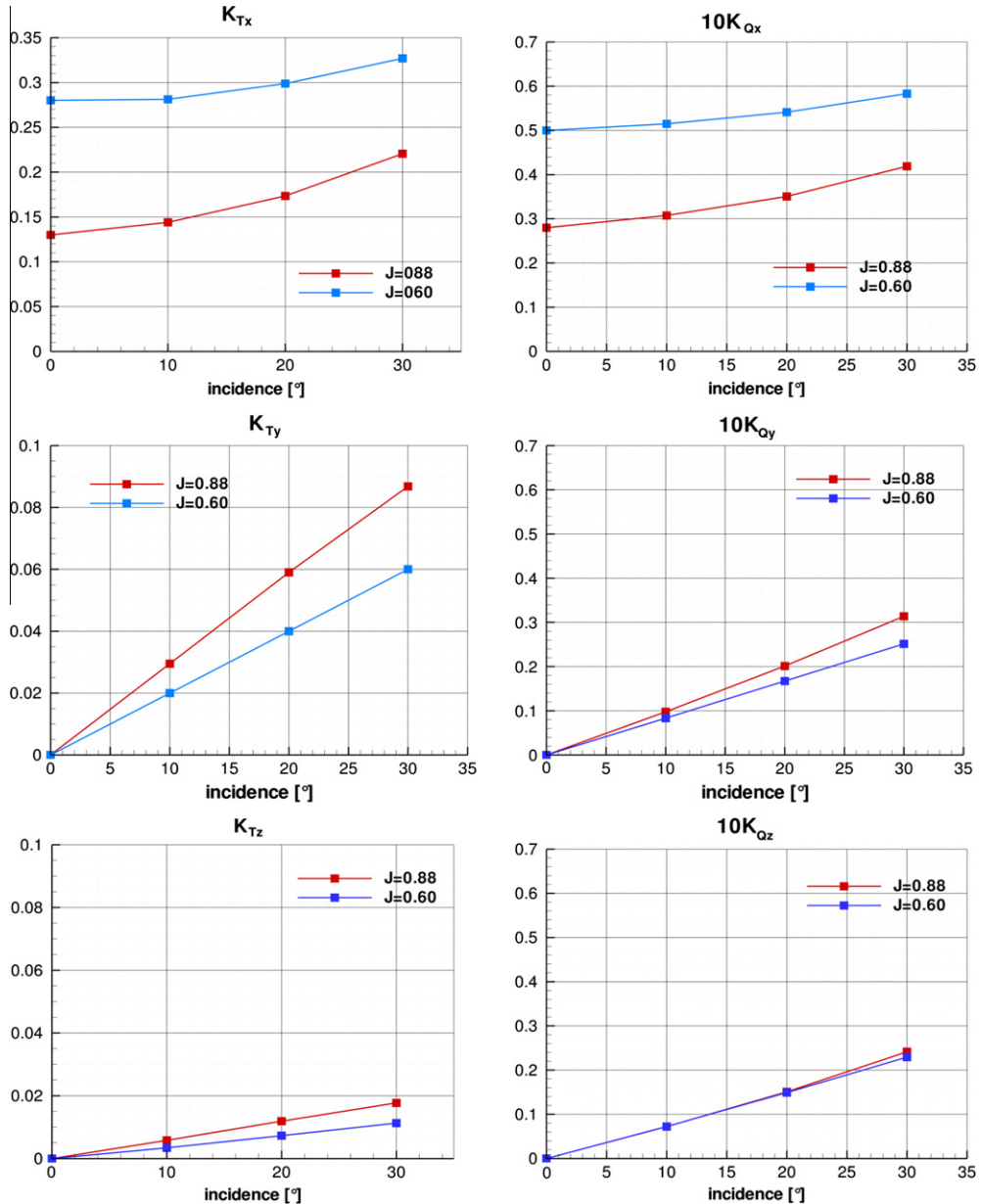
Fig. 4. Comparison of numerical results and experiments in open-water tests (— thrust; — torque; — efficiency).

of lateral and rotational speed result in low drift angle in correspondence of the propeller location); after the first phase, hull speed reduction and coupled sway-yaw motion cause the propeller to operate at low advance coefficient and at high incidence with respect to the mean flow, that is at a regime represented by the second fine grid simulation. Fig. 1 shows the inertial frame of reference adopted for the numerical simulations: the x axis, point-

Table 4
Propeller loads (medium grid).

β°	K_{Tx}	K_{Ty}	K_{Tz}	$10 * K_{Qx}$	$10 * K_{Qy}$	$10 * K_{Qz}$	η
<i>J = 0.88</i>							
0	0.1334	~ 0	0	0.2988	~ 0	~ 0	0.625
10	0.1440	0.0295	0.0058	0.3075	0.0978	0.0720	0.656
20	0.1734	0.0590	0.0119	0.3505	0.2013	0.1507	0.693
30	0.2205	0.0868	0.0177	0.4190	0.3136	0.2414	0.737
<i>J = 0.60</i>							
0	0.2693	~ 0	~ 0	0.5038	~ 0	~ 0	0.510
10	0.2812	0.0200	0.0034	0.515	0.0834	0.0725	0.521
20	0.2988	0.0401	0.0073	0.5413	0.1672	0.1491	0.527
30	0.3269	0.0600	0.0113	0.5833	0.2514	0.2295	0.535

ing downstream, coincides with the propeller axis of rotation; z axis is directed upward and the y axis follows the right hand rule. In the numerical simulations, the rotational speed of the propeller has been kept fixed to a value of $n = 25$ rps; the different values of the advance coefficients J are obtained by changing the resultant inflow velocity $U_\infty = \sqrt{(u_\infty^2 + v_\infty^2)}$; the oblique flow conditions have been achieved by varying the resultant angle of attack in the horizontal plane $x - y$, namely setting $u_\infty = U_\infty \cos \beta$ and $v_\infty = U_\infty \sin \beta$. Unless otherwise specified, all quantities have been cast in non-dimensional form by using as reference values the propeller radius ($L_{ref} = 0.1135$ m), the velocity of the blade tip ($U_{ref} = n\pi D \approx 17.85$ m/s) and the density of fluid ($\rho = 1000$ kg/m³). Therefore the non-dimensional period of revolution is $T = 2\pi$. The Reynolds number is the same of the physical

**Fig. 5.** Propeller loads (medium grid).

experiment carried out in pure axial flow conditions, i.e. $Rn = U_{ref}L_{ref}/v = 1.78 \times 10^6$.

5. Computational mesh

The computational mesh adopted in the numerical simulations consists of 75 overlapping blocks for a total of about 11.3 million volumes. A multigrid technique is exploited in order to achieve a faster convergence of the inner (pseudo-time) iteration, so four levels of computational mesh are used. Each level is obtained from the finer one by removing every other vertex along each spatial direction. Details of the cells distribution for the finest, medium and coarse discretization levels are listed in Table 3. The physical domain has been divided into three different zones: propeller and near wake field, buffer region and background. In Fig. 2 the building blocks of the mesh are represented: each blade, both fore and aft parts of the hub have been represented by an “O-grid” topology, whereas the rest of the mesh is made up by concentric

toroidal blocks that cover the whole computational domain. For the sake of clarity on the mesh strategy followed, three different slices in the planes $x = 0$, $y = 0$ and $z = 0$ are represented in Fig. 3; in particular, cells are clustered up to five radii in the downstream direction, where it can be expected that the peculiar features of the flow be resolved accurately (tip and hub vortices). Grid distribution is such that the thickness of the first cell on the wall is always below 1 in terms of wall units ($y^+ = O(1)$), the boundary layer being described by about 32 cells. Apart from the blocks fitted around the geometry, most of the cells are placed in the toroidal blocks that are used to track the propeller wake; moreover, the buffer toroidal block is used to improve grid overlapping quality between the near wake and the background. It has to be observed that, in order to achieve a mesh distribution aligned with the mean flow of the propeller slipstream in the horizontal plane $x-y$, the near wake mesh has been set at a different (lower) angle with respect the orientation of the inflow speed U_{inf} and the background. Finally, the time step has been set to $\Delta t \leq 0.01745$, corresponding to a rotation of one degree for the propeller blade, in the case of the finer grid.

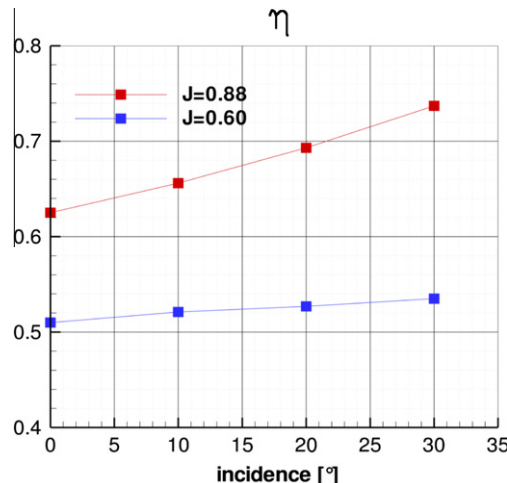


Fig. 6. Propeller efficiency (medium grid).

6. Results

Numerical results are mainly focused on forces and moments generated by the propeller; in order to explain the essential features of the phenomenon, pressure distribution on the blade and representative propeller sections during a complete cycle will be

presented. For the sake of completeness, moreover, the principal features of the downstream wake will be briefly described in terms of velocity and vorticity distributions. Unfortunately, due to the lack of experimental data in oblique flow conditions, validation of the numerical results has not been performed. It has to be remarked, however, that excellent agreement with experimental results has been obtained by the same numerical methodology for analyzing a similar propeller in pure axial flow condition [33] and behind a fully appended hull [32,34,12], both in terms of global loads and flow field features in the downstream wake.

In the following description, propeller forces (subscript T) and moments (subscript Q) have been non-dimensionalized as follows:

$$K_{Ti} = \frac{T_i}{\rho N^2 D^4} \quad K_{Qi} = \frac{Q_i}{\rho N^2 D^5} \quad (9)$$

where $i = x, y, z$ indicate the axis of the inertial frame of reference. Moreover, the propeller efficiency has been evaluated for all cases by the following relation:

$$\eta = \frac{JK_{Tx}}{2\pi K_{Qx}} \quad (10)$$

6.1. Pure axial flow condition

Results of numerical simulations performed for the propeller functioning in pure axial flow conditions are briefly summarized.

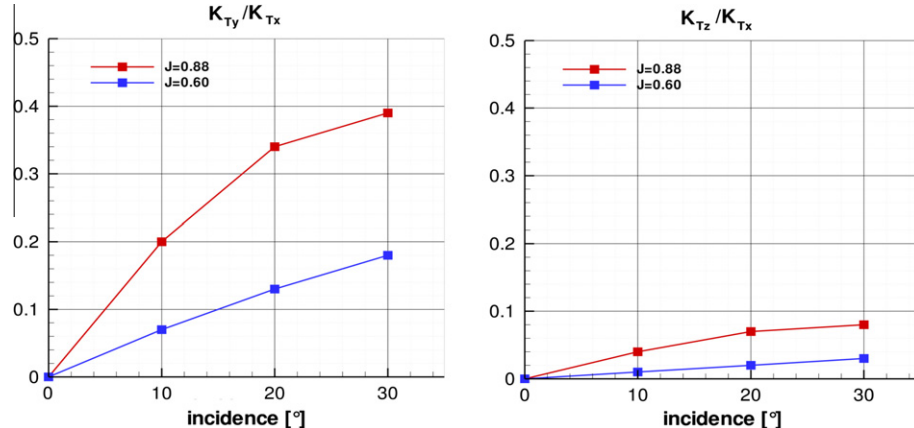


Fig. 7. Lateral and vertical forces ratio (medium grid).

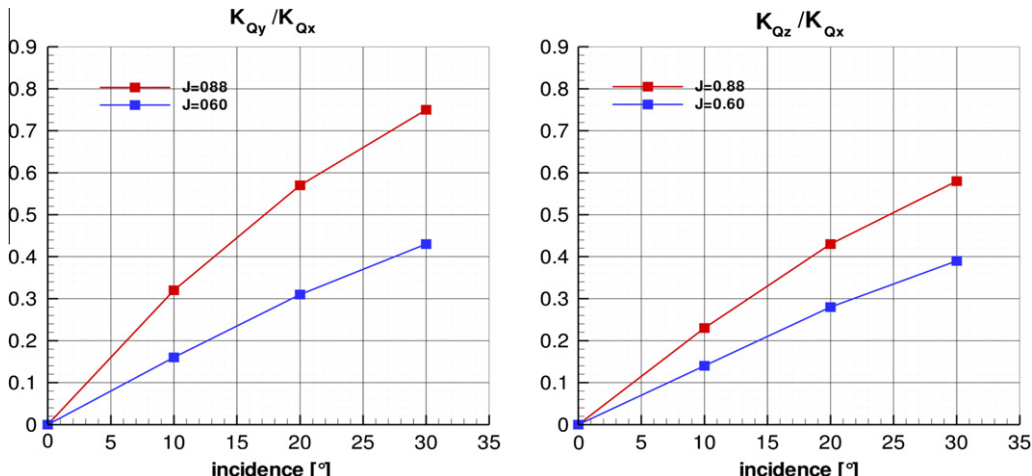


Fig. 8. In-plane pitching and yawing moments (medium grid).

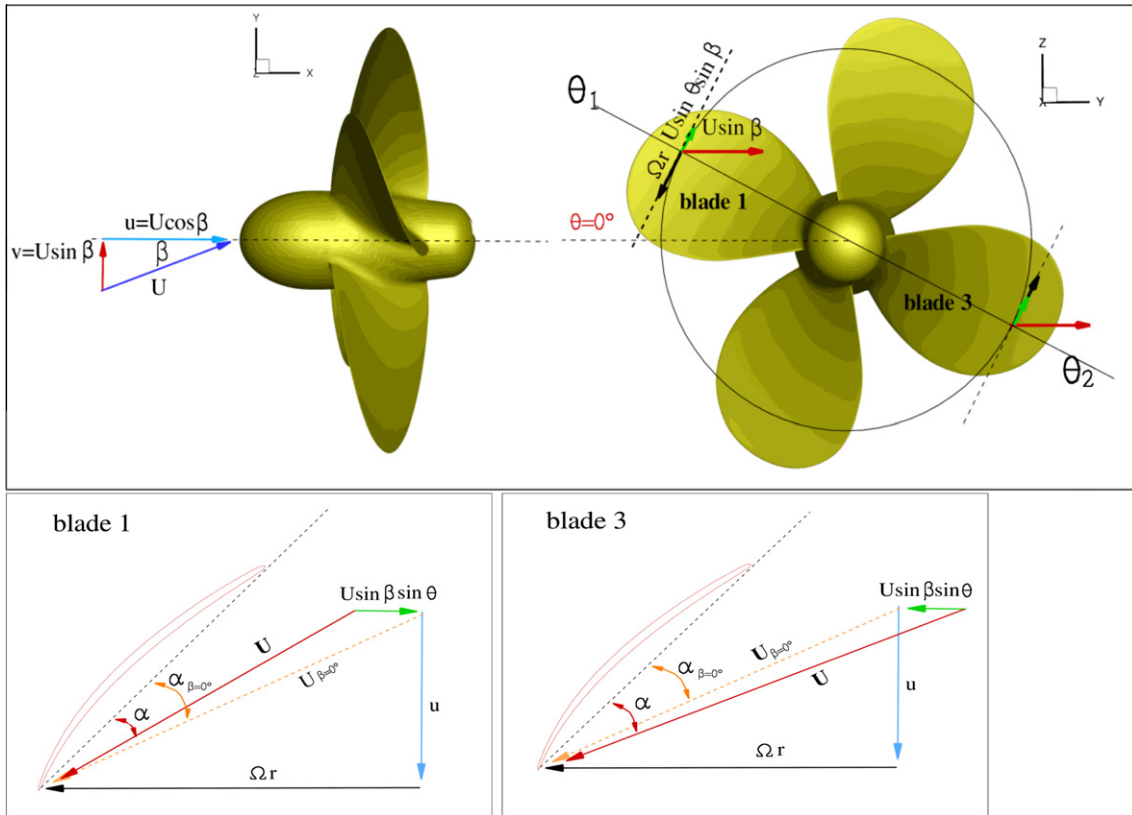


Fig. 9. Propeller blade section hydrodynamics in oblique flow.

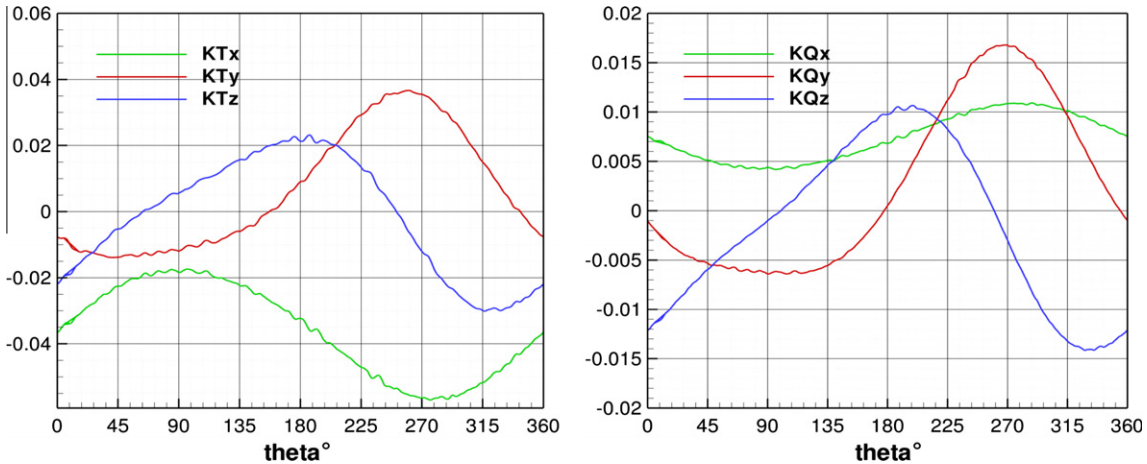


Fig. 10. Forces (left) and moments (right) developed by one blade ($J = 0.88$, $\theta = 10^\circ$). Hub frame of reference.

In Fig. 4 numerical results in terms of thrust and torque are compared to the experimental open water curves for a broad range of advance coefficient. The results for the fine grid are shown together with the relative error bars. The difference between computed and measured thrust is almost constant for all J s, i.e. it is smaller in percentage at low values of J (being about 4% of the experimental value) and grows with J up to a difference of about 15% for $J = 0.88$, where both the computed and the measured values of the force become very small. It is worth to note that the uncertainty bars reported on the numerical values are very small; in fact, the thrust estimated on the medium grid is almost identical to the value on the fine grid. On the contrary, the torque shows a greater sensitivity to mesh refinement, its value being strongly dependent on a

correct estimation of the viscous forces in the boundary layer. In particular, it can be noticed a shift of the whole curve towards lower values as the grid gets finer. In any case, the experimental data fall within the range of numerical uncertainty.

6.2. Oblique flow condition

6.2.1. Hydrodynamic loads

Propeller E779A performance in oblique flow has been assessed on the medium grid and results are listed in Table 4 in terms of absolute values of forces, moments and efficiency (defined in Eq. (10)); the same data, for the sake of clarity, are plotted in Figs. 5 and 6. The behavior of the propeller is qualitatively similar for

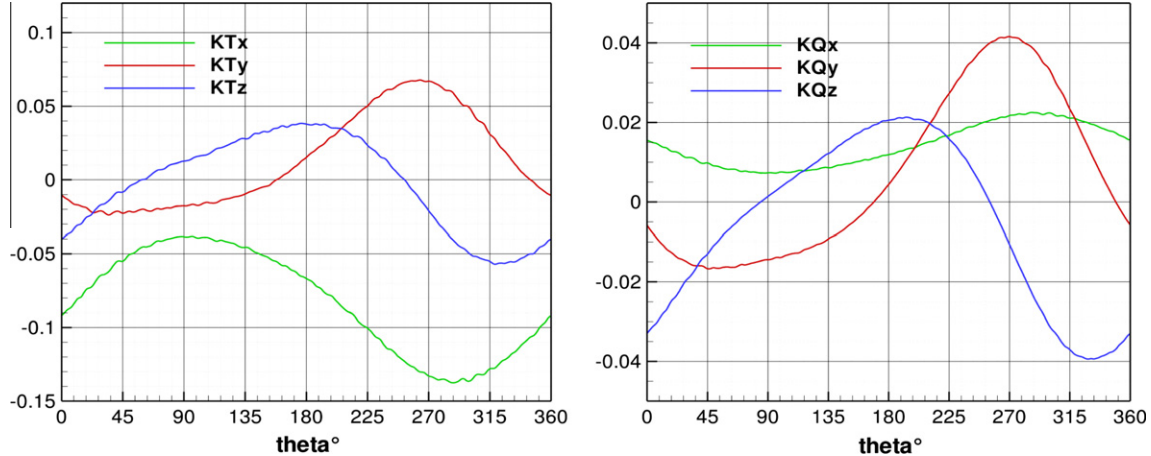


Fig. 11. Forces (left) and moments (right) developed by one blade ($J = 0.60$, $\theta = 30^\circ$). Hub frame of reference.

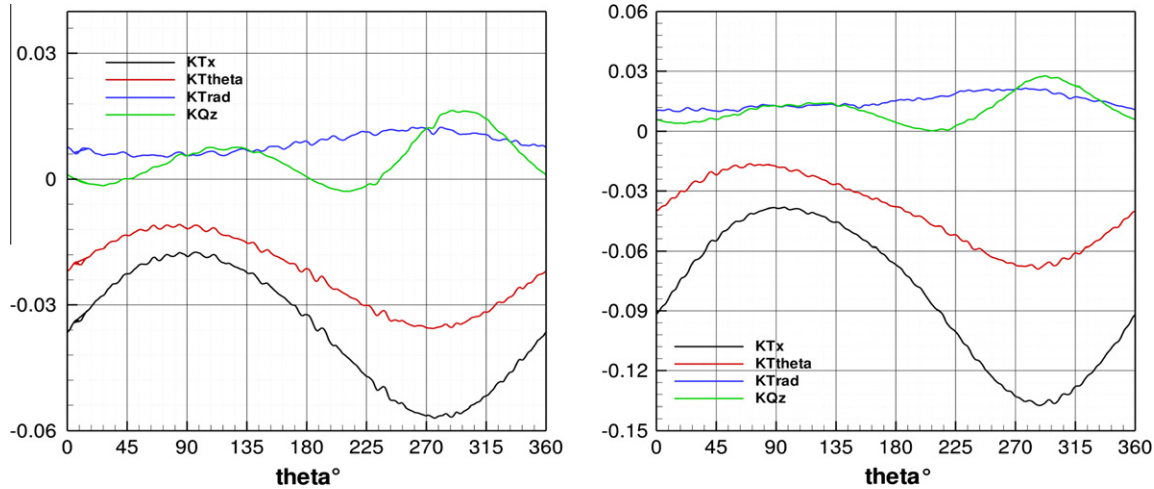


Fig. 12. Blade forces and spindle torque (Left: $J = 0.88$, $\theta = 10^\circ$; Right: $J = 0.60$, $\theta = 30^\circ$). Blade frame of reference.

the two loading conditions: both thrust and torque increase with drift angle, and moreover, this being the key aspect of present investigation, relevant forces and moments are generated in the propeller plane due to the asymmetric inflow conditions. In particular, the propulsive components, namely thrust (K_{Tx}) and torque (K_{Qx}), increase up to 65% and 21%, respectively, for the higher advance coefficient ($J = 0.88$), and up to 40% and 20% for the lower one ($J = 0.60$). Focusing on the in-plane loads, the most relevant component of the resultant force lies in the horizontal plane and is oriented in the same direction of the incoming flow, whereas the vertical one is much smaller. Moreover, moments in the horizontal and in the vertical plane (pitching and yawing moment, respectively) consist of a relevant percentage of the propeller torque. It is worth of note the different trend of propeller efficiency as a function of incidence angle for the two loading conditions; probably, moving from the light (close to the design condition) to the high loading condition, the viscous effects (strictly related to torque K_{Qx}) increase with respect to pressure effects (related to thrust, see Eq. (10)). Likely, at the highest J , the pressure loads increase faster than the viscous effects (i.e. efficiency increase with the incidence angle), whereas at the lowest J the trend of efficiency shows that they grow at a similar rate (that is its slope is constant). In Figs. 7 and 8 in-plane forces and moments are reported, in an alternative fashion, as percentages of longitudinal thrust and torque, respectively.

In order to provide a reliable support for synthesizing the numerical results that will be presented, the functioning of a propeller running at incidence with respect to the flow is described by analyzing the flow past a generic blade section during a complete revolution. To this aim, velocities in the inertial frame of reference have been projected on a frame moving with the blade; as it can be evidenced in Fig. 9, the blade section inflow consists of axial and circumferential components, defined as:

$$\text{axial component : } u_{\text{axial}} = U_\infty \cos \beta$$

$$\text{circumferential component : }$$

$$v_{\text{tangential}} = v_\Omega + v_\beta = \Omega r - U_\infty \sin \beta \sin \theta \quad (11)$$

where θ is the azimuthal position, Ω is the propeller rate of revolution, and r is the radial position of the blade section. In particular, the axial component and circumferential one, related to the propeller rotational velocity (i.e. $v_\Omega = \Omega r$), are constant (neglecting self induction velocity for the former one), whereas the component related to the transverse mean flow (i.e. $v_\beta = -U_\infty \sin \beta \sin \theta$) changes during a cycle, leading to a variable (geometric) angle of attack:

$$\text{geometric incidence : } \alpha = \Theta - \arctan \left(\frac{v_{\text{tangential}}}{u_{\text{axial}}} \right) \quad (12)$$

where Θ is the airfoil geometric pitch angle. Starting from the position at $\theta = 0^\circ$, the circumferential component follows a sinusoidal

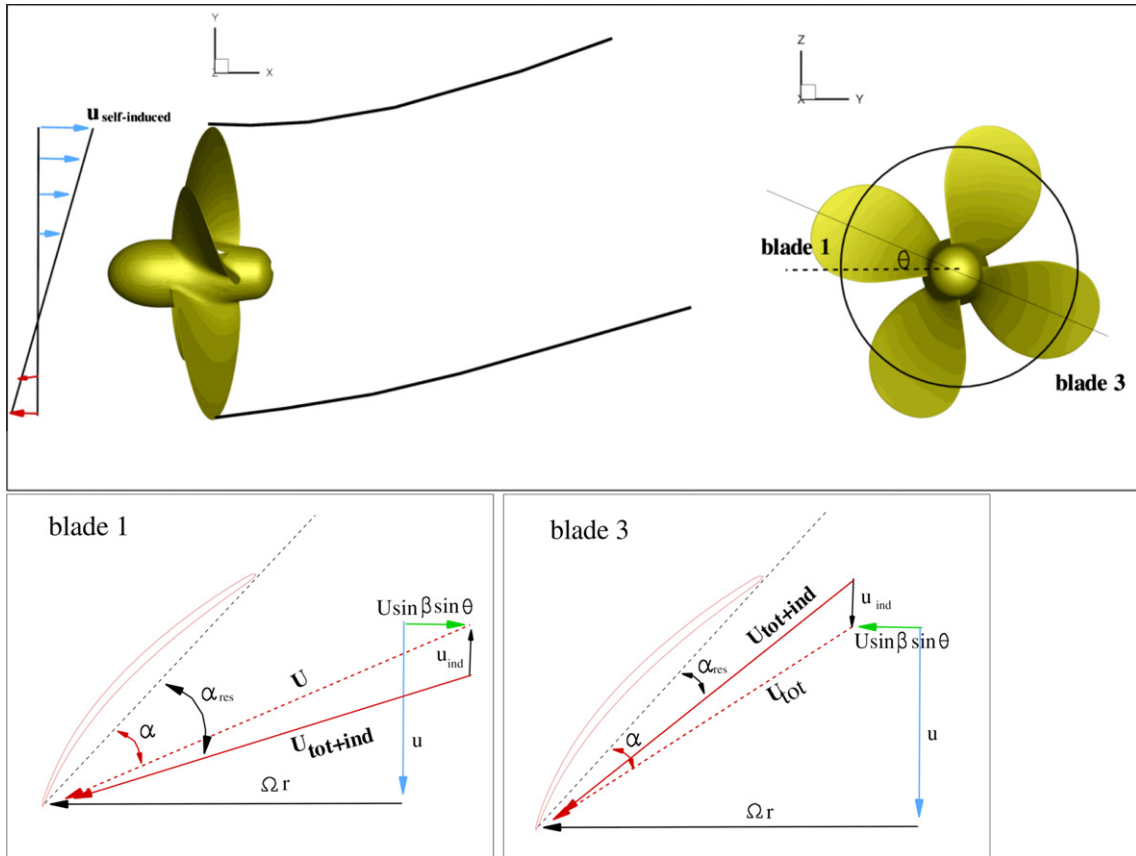


Fig. 13. Effect of wake deflection on the self-induced velocity distribution.

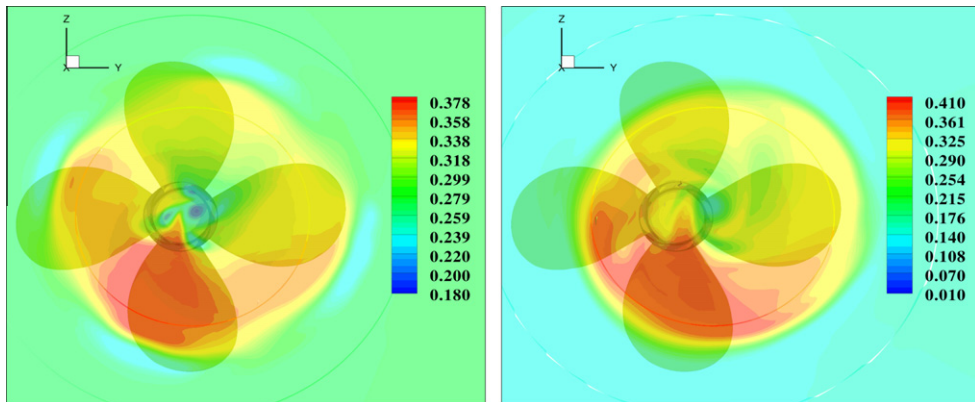


Fig. 14. Longitudinal velocity in the horizontal plane. Left: $J = 0.88, 10^\circ$. Right: $J = 0.6, 30^\circ$.

variation, with the minimum at $\theta = 90^\circ$, and the maximum at $\theta = 270^\circ$. In order to emphasize the role of the transverse component in the variation of the angle of attack, the blade section hydrodynamics has been sketched in Fig. 9 in correspondence of two generic blade angles (θ_1 and θ_2) and compared to the case of pure axial flow condition (subscript $\beta = 0^\circ$). In the former case, the angle of attack is reduced with respect to a pure axial flow condition because v_Ω and v_β are oppositely directed, causing a reduction of the resultant transverse component; on the other hand, for $\theta = \theta_2$ the two terms have the same sign and, consequently, the angle of attack is greater than the case $\beta = 0^\circ$.

As a direct consequence of the non-uniform inflow, the loads generated by the blade are not constant during the revolution, this

being the principal reason for the presence of forces and moments in the propeller plane. This behavior can be evidenced in Figs. 10 and 11, representing blade forces and moments in the hub frame of reference (i.e., the inertial one) for $J = 0.88$ (10°) and $J = 0.60$ (30°). For both loading conditions, the wave form of the loads mirrors the harmonic variation of the inflow. The thrust K_T and the lateral force K_Ty developed during the blade passage on the upper half of the disk ($0^\circ < \theta < 180^\circ$) are lower with respect to those developed in the lower half; moreover, close to $\theta = 270^\circ$, their maximum values show a slight phase shift. In this regard, it has to be observed that the thrust component is mainly affected by the pressure field developed on the blades, whereas the side force is mainly related to viscous effects confined in the boundary layer; as a con-

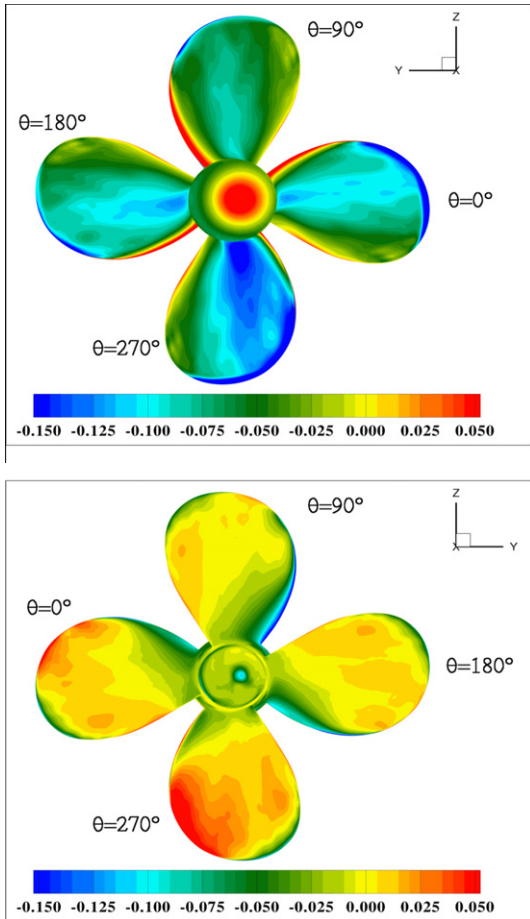


Fig. 15. Pressure field on propeller blades ($J = 0.88$ at 10°). Up: suction side. Down: pressure side.

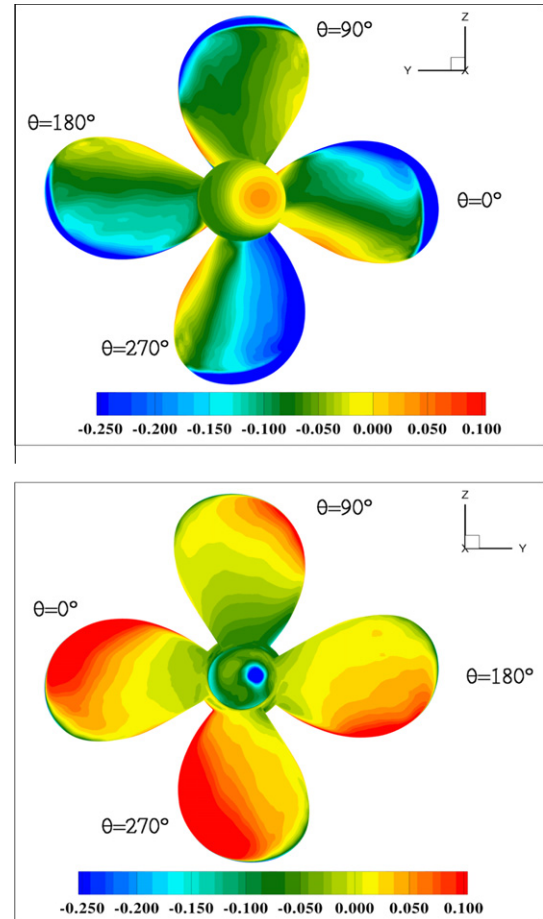


Fig. 16. Pressure field on propeller blades ($J = 0.60$ at 30°). Up: suction side. Down: pressure side.

sequence, the different time response of the pressure variation over the blade with respect to the boundary layer development due to the varying inflow experienced by the rotating blade, would originate this lag [35,36]. The vertical component K_{Tz} is phase-shifted with respect to the other components by a quarter of cycle (i.e. $\pi/2$); it is worth to note that, despite the fact that vertical velocity component of the inflow is zero, the resultant average value of K_{Tz} (smaller than the K_{Ty} component) is not, as a result of the non-homogeneous distribution of the self-induction velocity over the propeller disk [37]. In fact, the circulation convected with the trailed and shed vortex system is different for each blade as a consequence of the variable inflow experienced during a revolution (see Eq. 11 and Fig. 9) and, therefore, the induced velocity field is distributed in a non-symmetric fashion. Moreover, because of the inclination of the propeller slipstream with respect to the propeller rotational axis, a negative induced velocity field (i.e. up-wash) is generated over the propeller disk which further amplify the non-uniform propeller loading distribution. The effect of the propeller slipstream deflection on the blade loads is schematically described in Fig. 13, where the hydrodynamics of a generic blade section at the same positions close to $\theta = 0^\circ$ and $\theta = 180^\circ$ is described. It is evident that the deflection of the propeller wake causes negative induced velocities u_i in the outer portion of the first and fourth quadrant of the propeller disk; on the contrary, the self-induction is more concentrated on the opposite side, where the vortex tube is deflected. As a consequence, in the former position, the up-wash further amplifies the effects of the transverse component v_β , i.e., the angle of incidence is further increased. The opposite trend is

schematized near $\theta = 180^\circ$, where the angle of attack is reduced due to the increase of the axial velocity component. In order to further investigate this aspect, in Fig. 14 a transverse section of the downstream wake of the propeller at $x = 0.5$, is represented in terms of the longitudinal component u ; this visualization allows to detect the circumferential position where the propeller imparts to the fluid the strongest acceleration, and consequently, the location where the highest loading is experienced by each blade. It should be emphasized that the distribution of the propeller load is shifted with respect to the vertical axis towards the fourth quadrant of the propeller plane ($270^\circ < \theta < 0^\circ$), contrarily to what should be expected as the sole outcome of the simplified relation expressed in Eq. 12 that identifies $\theta = 270^\circ$ as the location with the maximum inflow angle (“averaged” over all the blade sections). As a consequence, K_{Tz} generated between $\theta = 90^\circ$ and $\theta = 270^\circ$ is lower with respect to the one generated in the remaining half ($270^\circ < \theta < 90^\circ$), the resultant mean value being oriented in negative z direction. On this basis, it is straightforward to clarify the features and the nature of the blade moments: the eccentricity of the loads, and, in particular, of the thrust K_{Tx} in fourth quadrant, generates a positive pitching moment K_{Qy} and a negative yawing moment K_{Qz} . Finally, the contribution of the hub to the global loads exerted on the complete propeller is negligible with respect to the ones due to the blade, both in terms of forces and moments. In Fig. 12 blade loads components in a reference frame fixed to the blade are reported.

It is worthy of notice that the “spindle” torque, namely the torque oriented along the blade span direction, denotes a wavy

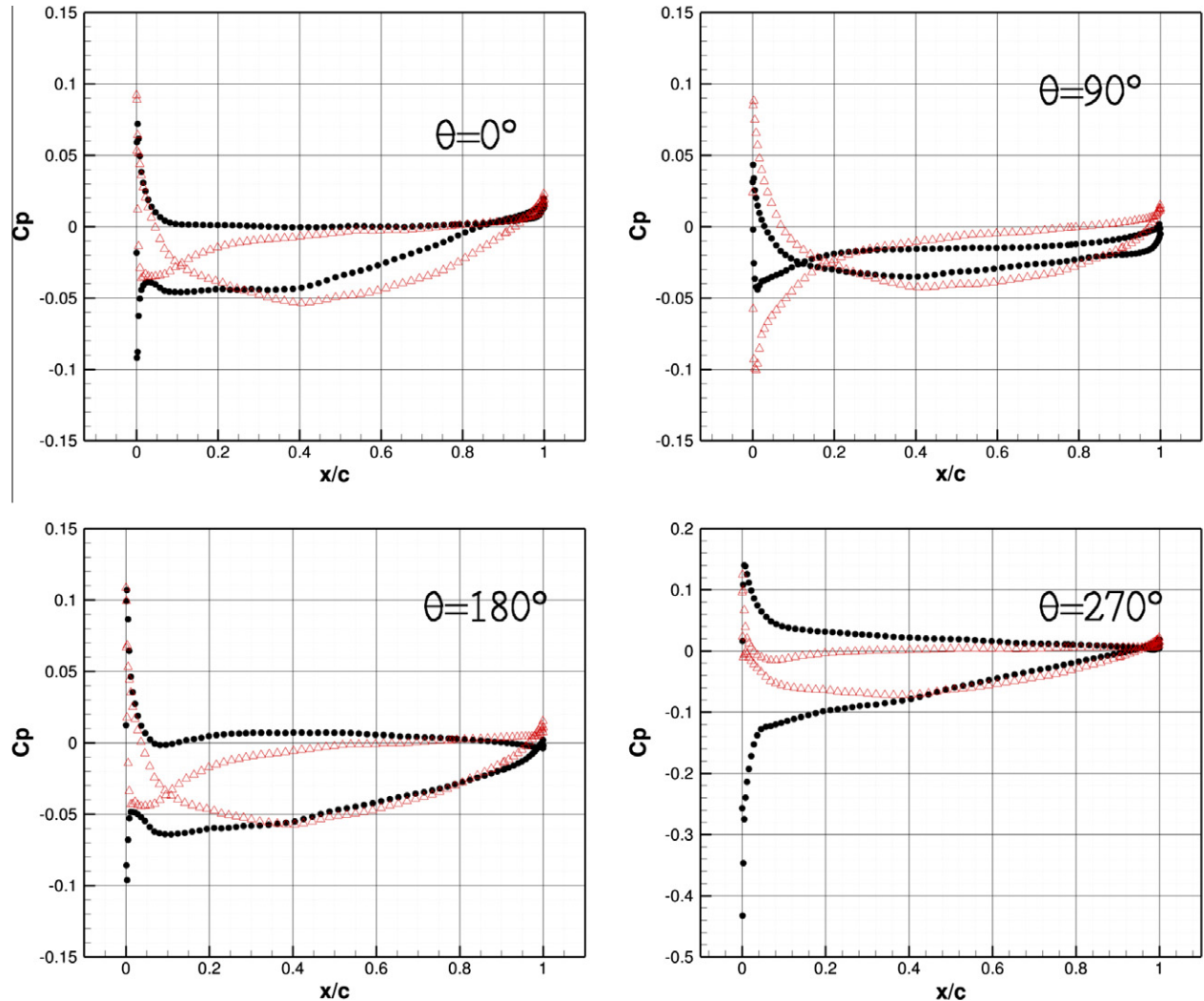


Fig. 17. Comparison of C_p at blade section $\frac{r}{R} = 0.4$. $\Delta: J = 0.88, 10^\circ$, $\bullet: J = 0.60, 30^\circ$.

variation with an higher harmonic content than the forces. Moreover, the two loading conditions have different characteristics: at the lowest J , the moment experiences two different sign inversions for two short intervals, probably because at this conditions the center of pressure of the blade is located at an higher distance from the leading edge with respect to the $J = 0.88$ case. Pressure field description in next section will provide a further support and a finer overview of the different hydrodynamic behavior of the blades at both advance coefficients.

6.2.2. Pressure and wake field

The pressure field developed on the blade and on representative blade sections during a revolution is described in order to gain a better insight into the nature of the loads generated in oblique flow conditions. The following discussion is centered on the same conditions analyzed with the finest grid resolution ($J = 0.88$ and $J = 0.60$ at incidence of 10° and 30° , respectively). Moreover, the main features of the propeller wake will be discussed in terms of velocity and vorticity distribution on the horizontal plane $z = 0$. In Figs. 15 and 16 the pressure generated on the propeller blades, at prescribed circumferential locations, are visualized for the two advance coefficients in terms of $C_p = \frac{p}{\frac{1}{2}\rho U^2}$. It has to be pointed out that blade positions are represented in the same frame of reference considered for the hub loads (Figs. 10 and 11). In both cases, the pressure field has a behavior consistent with the trend of the

angle of attack defined in Eq. 12. At $\theta = 90^\circ$, as already shown in Figs. 10 and 11, the blade is in the lowest loaded condition and this is confirmed by the relatively small intensity of the pressure on its surface; on the contrary, at $\theta = 270^\circ$ the pressure intensity is highest on relevant portion of the pressure and suction sides of the blade. Considering the two horizontal positions, $\theta = 0^\circ$ and $\theta = 180^\circ$, slight asymmetries in the pressure field are evident at $J = 0.88$ on the pressure side. On the other hand, with the increasing of propeller loading, the asymmetry of pressure distribution with respect the z axis is more evident; in particular, at $\theta = 0^\circ$, the pressure intensity on the front and back side of the blade is higher, and moreover, extended on a wider portion, with respect the one experienced at $\theta = 180^\circ$. This general overview of the pressure distribution further explains the nature of the in-plane loads (in the hub frame of reference) developed by a propeller working in oblique flow: the different pressure distributions along the vertical axis generate the positive side force and pitching moment; on the other hand, the pressure distribution along the horizontal axis generates the vertical force and the yawing moment. Moreover, it should be stressed that the former effect is mainly due to the lateral component of the inflow, whereas the latter one is a consequence of the three-dimensional self induction effects, as described in the previous section.

In order to provide a better description of the pressure field developed for the two advance coefficients, the pressure coefficient

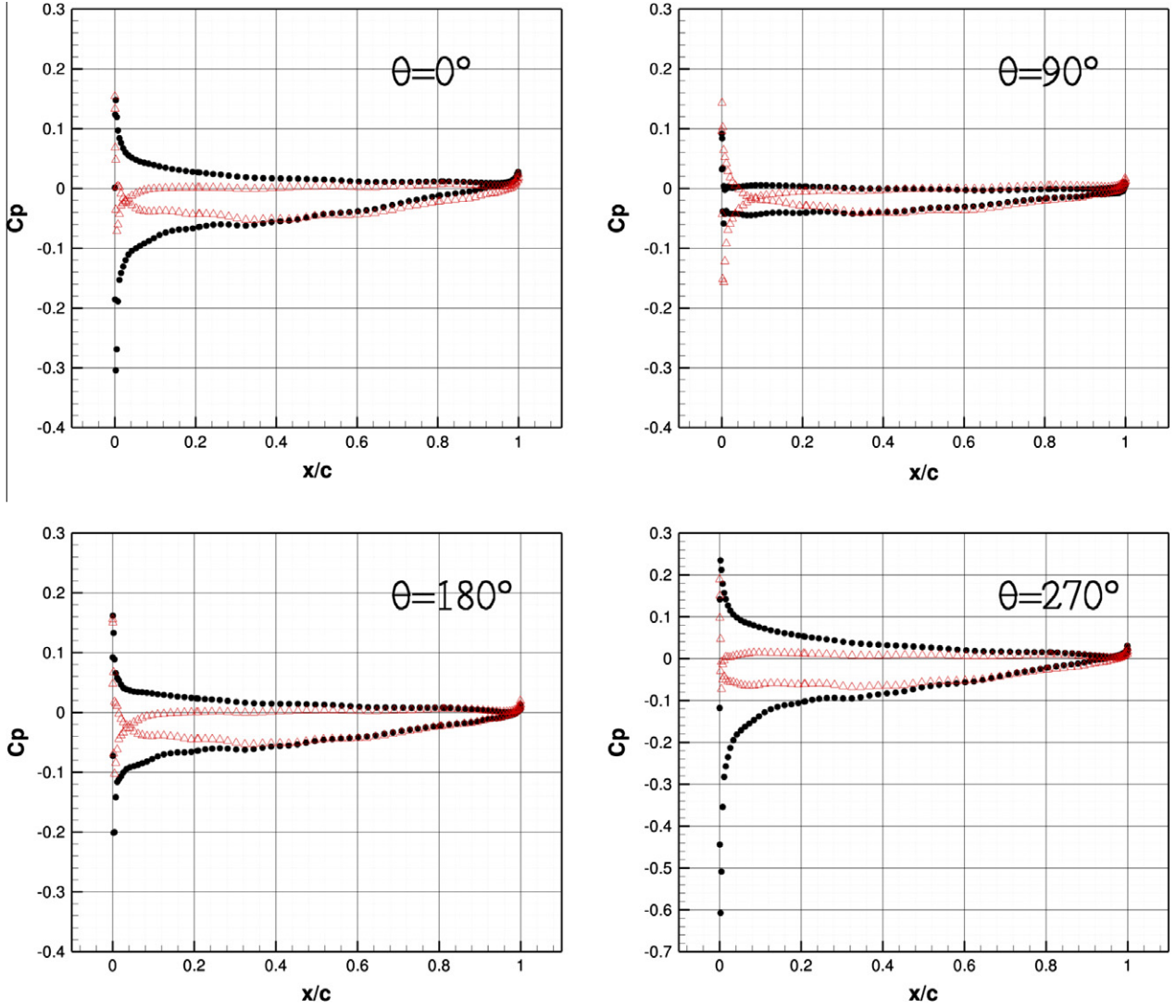


Fig. 18. Comparison of C_p at blade section $\frac{r}{R} = 0.6$. Δ : $J = 0.88$, 10° , \bullet : $J = 0.60$, 30° .

distribution of blade sections at $r/R = 0.4$, $r/R = 0.6$ and $r/R = 0.8$ (representative of the root, middle and tip portion of the blade, respectively) during a revolution are compared in Figs. 17–19. The blade section at $r/R = 0.4$ (Fig. 17) at the highest advance coefficient ($\beta = 10^\circ$) experiences a negative angle of attack during the complete cycle, as it is evident by the change in sign (and overlapping of the profiles near the leading edge portion, i.e. $x/c < 0.2$). The extent of the overlapping portion reaches a maximum at $\theta = 90^\circ$, whereas at the two horizontal positions is reduced approximately by a factor of 2 ($x/c < 0.1$); the overlapping disappears at $\theta = 270^\circ$. Considering the lowest J , on the other hand, the angle of attack is negative only at $\theta = 90^\circ$ only, the C_p overlapping region being less wider than for the previous case. This phenomenon is mainly caused, or at least amplified (with respect to the axisymmetric conditions), by the transverse component of flow which modifies the transverse component impinging on the blade section and, therefore, the local incidence (see Eq. 12). This different behavior can be clearly detected by observing Figs. 15 and 16: in the former one, an inversion of pressure sign over the leading edge is evident up to the sections at mid-span, except for $\theta = 270^\circ$, where it is exclusively confined near the hub; on the contrary, this effect is only evidenced at $\theta = 90^\circ$ at $J = 0.60$. Blade section $r/R = 0.6$ at $J = 0.88$ confirms a similar behavior (see Figs. 15 and

18), i.e. pressure sign inversion at the leading edge; however, the extent of the inverted sign region of C_p is substantially reduced. At $J = 0.6$, the section always works at positive incidence; moreover, it should be observed the presence of an intense suction peak at $\theta = 270^\circ$, three times larger than the peak on the pressure side. Finally, Fig. 19 shows the behavior of the blade section $r/R = 0.8$. At both loading conditions, the section works at positive incidence angle, as confirmed by the absence of a change in the sign of the pressure on the back and suction side of the blade; however, it should be noticed the markedly different working behavior at the two advance coefficients: at $J = 0.88$, the section develops similar pressure and suction load at the leading edge; on the contrary, at $J = 0.6$ the suction peak is greater up to one order of magnitude (at $\theta = 270^\circ$) than the stagnation pressure on the face.

For the sake of completeness, characteristics of the propeller wake is described in terms of absolute velocity and the vertical vorticity component in the horizontal plane ($V_{xy} = \sqrt{u^2 + v^2}$ and $\omega_z = \frac{dv}{dx} - \frac{du}{dy}$, respectively). In Fig. 20 the velocity field in the wake is reported for $J = 0.88$ (up) and $J = 0.60$ (down); it can be observed that the energy imparted to the flow is higher in the negative y side ($\theta = 0^\circ$), due to the eccentricity of the propeller loads located in the fourth quadrant ($270^\circ < \theta < 0^\circ$). It should be observed that, at the lowest loading condition, the trailing vortex system is tracked up

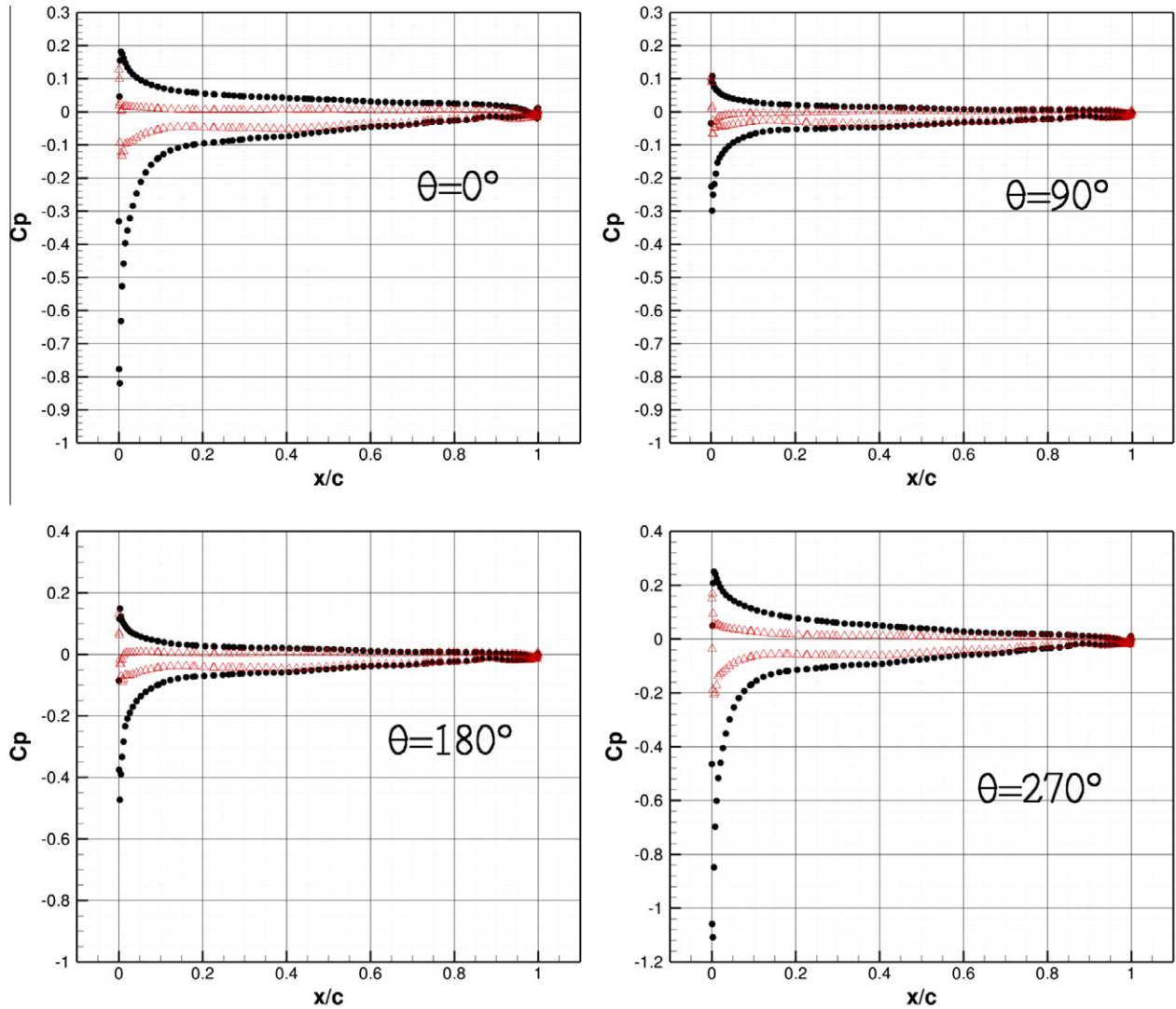


Fig. 19. Comparison of C_p at blade section $\frac{r}{R} = 0.4$. Δ : $J = 0.88$, 10° , \bullet : $J = 0.60$, 30° .

to the end of the near wake domain (about three times the propeller diameter D), and interaction among the vortex lines seems to be negligible. On the other hand, at the highest loading condition, the resolution of the trailing vortex system is poorer because of strong interaction among the vortex lines, which amplify also diffusion effects. The different wake field behavior at the two loading conditions can be further appreciated by analyzing the vertical component of vorticity (Fig. 21): at $J = 0.88$, no destabilization or interactional phenomenon of the trailing vortex system is evidenced; on the contrary, at $J = 0.60$, the combined effects of kinematics (convection speed or, alternatively, pitch of the trailing vortex system), loading conditions and mean inclination of the wake, may act in favor of interactions of trailing vortex and, consequently, their destabilization and diffusion, as it can be observed downstream at about one propeller diameter.

6.2.3. Grid convergence analysis

For the two test conditions analyzed, computations have been performed considering three different mesh resolutions, in order to get a rigorous evaluation of the numerical uncertainty. In Table 5 propeller loads are summarized for three grid levels. When following the procedure suggested in [38], grid convergence results with three grid level were poor, oscillatory convergence being observed in some cases. This is probably to be ascribed to the inability of the

coarse grid to resolve the main flow features. As a consequence, only results on the medium and fine grids have been taken into account to estimate grid convergence. In particular, the solution variation has been computed as:

$$E = \frac{f_2 - f_1}{1 - r^p} \quad (13)$$

where f_1 and f_2 are the solution on the fine and medium grid, r the refinement factor ($r = 2$, as stated before) and p is the “formal” order of accuracy ($p = 2$, for the present solver). Then, the uncertainty is evaluated by:

$$U_N = F_S |E| \quad (14)$$

where F_S is a safety factor assumed equal to 3, according to Roache.

Outcome of the grid convergence is summarized in Table 6: the uncertainty is lower than 5% for the propeller loads at both conditions, with the exception for the vertical component K_{Lz} ; it has to be pointed out, however, that this component is much smaller than the others, and consequently, the numerical solver and the grid strategy adopted can be regarded as successful in capturing the essential peculiar phenomena. As a final remark, it can be said that the propeller loads computed via the medium grid are very close to the finer grid results, and, for the purpose of performance prediction, can be considered reliable.

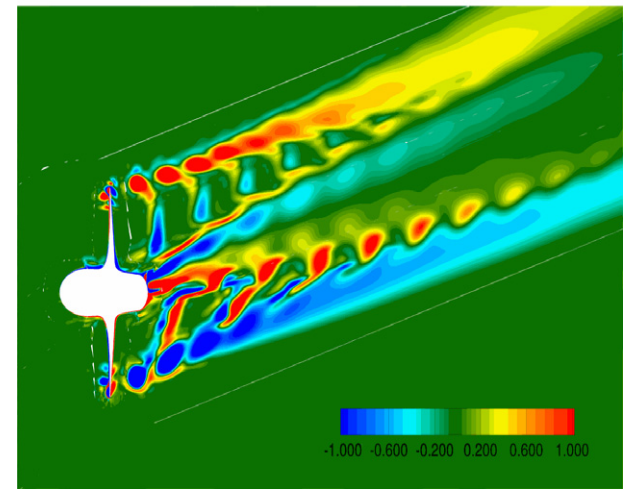
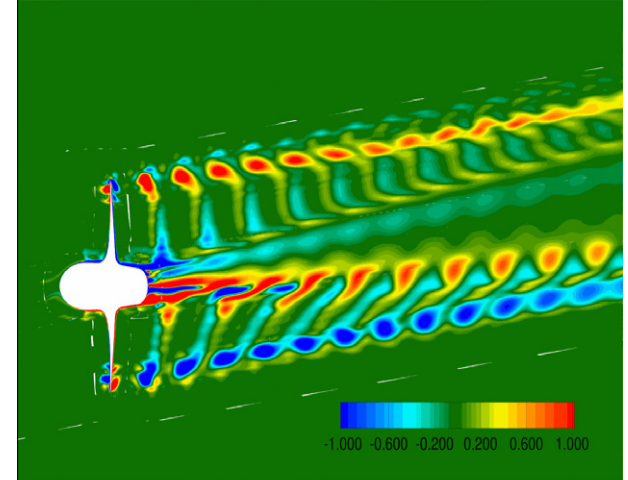
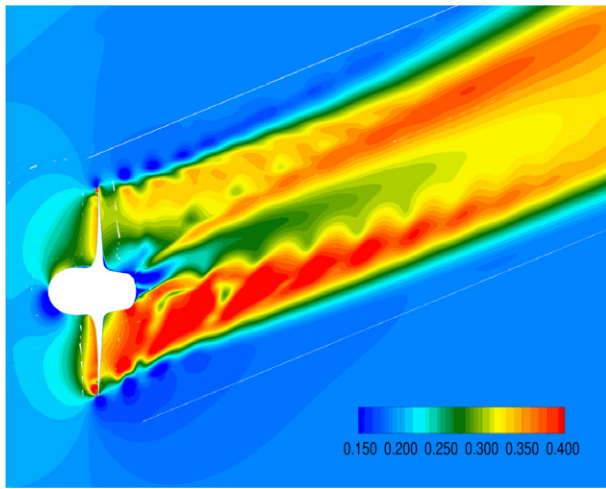
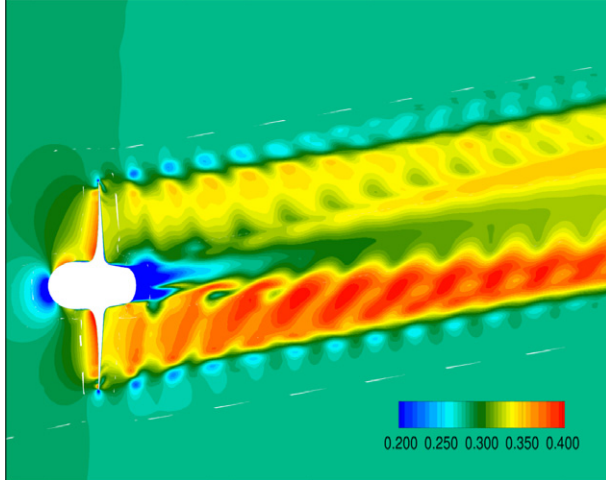


Fig. 20. Absolute velocity in the horizontal plane. Up: $J = 0.88$, 10° . Down: $J = 0.6$, 30° .

7. Conclusions

The INSEAN E779A propeller in oblique flow conditions has been investigated by means of a dynamic overlapping grid technique; in particular, a relative wide range of angle of incidence (up to 30°) has been considered for two propeller loading conditions, namely at moderate ($J = 0.88$) and at medium-high ($J = 0.6$) loading. The focus has been mainly centered on the behavior of the propeller in terms of global loads. As a result of the non-symmetric inflow condition, relevant in-plane loads, which are usually not of concern in pure axial flow condition or in hull-behind condition in straight ahead motion, are generated by the propeller. In particular, in a common off-design scenario of ship operation (i.e. maneuvering), these components may increase up to 20% of the thrust and 40% of the torque, for the side force and in plane moments (pitching and yawing), respectively. The description of the pressure developing on the blade during a complete revolution, the pressure distribution over different representative blade sections and the downstream wake in terms of velocity and vorticity fields, further supported the comprehension of force generation. Unfortunately, due to the lack of experiments in oblique flow conditions, a validation of the numerical computations has not been carried out; in this regard, however, it has to be remarked that the very accurate results obtained in open water tests (axisymmetric flow) and the low uncertainty evaluated by means of two grid levels in oblique test, can be considered a valuable support for

Table 5
Convergence results for the propeller loads.

	K_{Tx}	K_{Ty}	K_{Tz}	$10 * K_{Qx}$	$10 * K_{Qy}$	$10 * K_{Qz}$
$J = 0.88$						
Coarse	0.1397	0.0327	0.0036	0.3286	0.1004	0.0651
Medium	0.1440	0.0295	0.0058	0.3075	0.0978	0.0720
Fine	0.1418	0.0295	0.0070	0.2948	0.0976	0.0735
$J = 0.60$						
Coarse	0.3092	0.0653	0.0059	0.5792	0.2532	0.2082
Medium	0.3269	0.0600	0.0113	0.5833	0.2514	0.2295
Fine	0.3253	0.0575	0.0121	0.5650	0.2513	0.2285

the accuracy of present computations. It has to be stressed, moreover, that due to its intrinsic capability to provide a fine description of the flow field and consequently, a detailed insight into the underlying physical phenomena, CFD may be a valuable tool for the improvement and validation of low order propeller models, that can be a useful support to reduce the computational burden when simulating, for instance, the manoeuvre of a fully appended hull.

Acknowledgments

This work was partially supported by the Italian Ministry of Education, University and Research through the research project RITMARE. Numerical computations presented here have been

Table 6
Grid convergence analysis.

Load	Medium	Fine	E	Extr.	$U_N\%$
<i>J = 0.88</i>					
K_{Tx}	0.1440	0.1418	2.2e-3	0.1396	1.58
K_{Ty}	0.0295	0.0295	0.0	0.0295	0
K_{Tz}	0.0058	0.0070	-1.2e-3	0.0082	-14.63
$10 * K_{Qx}$	0.3075	0.2948	1.27e-2	0.2821	4.5
$10 * K_{Qy}$	0.0978	0.0976	2e-4	0.0974	0.21
$10 * K_{Qz}$	0.0720	0.0735	-1.5e-3	0.0750	-2
<i>J = 0.60</i>					
K_{Tx}	0.3269	0.3253	1.6e-3	0.3237	0.49
K_{Ty}	0.06	0.0575	2.5e-3	0.055	4.55
K_{Tz}	0.0113	0.0121	-8e-4	0.0129	-6.2
$10 * K_{Qx}$	0.5833	0.0565	1.85e-2	0.5463	3.39
$10 * K_{Qy}$	0.2514	0.2513	1e-4	0.2512	0.04
$10 * K_{Qz}$	0.2295	0.2285	1e-3	0.2275	0.44

performed on the parallel machines of CASPUR Supercomputing Center (Rome); their support is gratefully acknowledged.

Appendix A. Comparison with low order models

Numerical computations emphasized the capability of a sophisticated CFD method to perform high resolution analysis of the propeller in oblique flow; unfortunately, this approach is not a viable solution when a fully-appended hull has to be simulated, because the minimum time step discretization should be reduced in order to solve the propeller blade hydrodynamics, increasing prohibitively the computational resource demand. Instead of a direct solution, a convenient way is to model the physic of the propeller by means of low order models, like Blade Element Momentum Theory, Actuator Disk or Boundary Element Method (BEM).

With the increasing interests towards off-design conditions (i.e. various aspects of maneuvering), a reliable propeller model should mimic the peculiar hydrodynamic features in these conditions also. A promising approach for modeling propeller behavior in general maneuvering conditions, very cheap from the computational point of view, consists in the use of hybrid models, namely Actuator Disk with an in-plane force correction or Blade Element Momentum theory [7]. In order to check the capability of low order models in capturing oblique flow effects, numerical results have been compared to the outcomes of three different low order theories. It has to be remarked that, in this instance, only the propeller side force has been considered, because, as it has been extensively introduced in the above paragraphs, it plays a remarkable role in the ship dynamic behavior. In particular, three different lateral force models have been considered, namely Ribner theory [4], Gutshe method [39] and a modified Blade Element one [40]; it is not the purpose of present work to show the details of these models and coupling with CFD solvers, for which the interested reader is referred to the cited literature. Here, only the main features will be summarized. In all these models, simplified side force formulations are used. Ribner formulated the propeller side force by means of a hybrid model among blade element and momentum theory, in terms of a control derivative:

$$K_{Ty} = K_\sigma \frac{F(a)}{1 + k_a K_\sigma} k_s Z \beta \quad (\text{A.1})$$

where Z is the number of blades, β is angle of attack, K_σ is a constant proportional to the blade projected area in the side plane and $F(a)$ is the propeller load factor defined as:

$$F(a) = \frac{(1+a)[(1+a)+(1+2a)^2]}{1+(1+2a)^2} \quad (\text{A.2})$$

where a is the axial self-induction factor.

Table 7
Comparison of side force ratio among uRaNSe and simplified theories.

$\frac{K_{Ty}}{K_{Tx}}$	Gutshe	%Err.	Ribner	%Err.	BEMT	%Err.
<i>J = 0.88</i>						
10°	0.26	28.24	0.265	29.49	0.12	-37.82
20°	0.45	32.35	0.445	32.2	0.21	-37.83
30°	0.56	42.70	0.544	38.25	0.24	-37.67
<i>J = 0.60</i>						
10°	0.067	-4.78	0.076	6.5	0.041	-41.0
20°	0.1315	-1.73	0.144	7.5	0.078	-41.2
30°	0.19	3.92	0.20	9.08	0.10	-42.0

Gutshe theory is an attempt to estimate propeller side force by means of the propeller open water characteristics and assuming that the propeller may be described in terms of an “equivalent” blade section at $r/R = 0.75$; in particular:

$$K_{Ty} = \left[2K_{Qx}(J=0) - J \frac{dK_{Qx}}{dJ} \right] J \tan \beta \quad (\text{A.3})$$

Blade Element Momentum theory is based on the assumption that the global propeller loads can be obtained by integration of the loads generated by the blade sections, assuming that they do not interact with each other. Considering the 2D dimensional lift and drag properties of the blade sections, C_{Lx} and C_D , the side force can be evaluated by the following expression:

$$K_{Ty} = \frac{Z}{2\pi} \int_{r_0}^R \int_0^{2\pi} [C_{Lx} \alpha_{eff} \sin(\Omega - \alpha_{eff}) + C_D \alpha_{eff}] \sin \theta dr d\theta \quad (\text{A.4})$$

where α_{eff} is the effective angle of attack at each section and accounts also for the self-induction effect, Θ is the pitch angle of the section, θ is the azimuthal position, Z is the number of blades and r_0 is the hub radius; the double integration cover the radial direction (along the blade span) and circumferentially over the disk. In Table 7 side ratio of side force in percentage of the thrust are compared with the uRaNSe results for the two advance coefficient J considered in this study; it has to be remarked that in case of the Ribner's and the Gutshe's model, the ratio is computed with respect to the thrust calculated by the uRaNSe. Both models provide very similar results at both advance coefficients. In particular, the side force ratio is higher of more than 30% and increases up to 40% when increasing the incidence angle at the lowest loading condition; at $J = 0.6$, the results are very promising with an average error of about 3% and 8% for Gutshe's and Ribner's model, respectively. On the contrary, BEMT predicts a side force ratio of about 37% and 40% lower than the uRaNSe outcomes. It has to be stressed that in this case the ratio has been affected by discrepancies in the thrust magnitude provided by BEMT. The poorer ability of BEMT model can be attributed mostly to the inability to capture 3D effects and to the simplified assumptions of straight wake for the computation of self-induction effects. On the other side, Gutshe's and Ribner's model are superior with respect to the previous model, in particular in the medium-high propeller loading regime, whereas the absolute error is similar to BEMT, but with sign inversion, in the low loading regime. It can be stressed that uRaNSe computation may guide to a deeper investigation on this aspect; in particular, it can be a valuable tool for including proper corrections able to reproduce oblique flow effects into low order, computationally efficient, models.

References

- [1] Viviani M, Podenzana Bonvino C, Mauro S, Cerruti M, Guadalupe D, Menna A. Analysis of asymmetrical shaft power increase during tight manoeuvre. In: 9th International conference on high performance marine vehicles (FAST), Shanghai, China; 2007.

- [2] Coraddu A, Dubbioso G, Mauro S, Viviani M. Experimental investigation of asymmetrical propeller behaviour of twin screw ships during manoeuvres. In: Proc. of int. conf. on marine simulation and ship maneuverability MARSIM2012, Singapore; 2012.
- [3] Mauro S, Dubbioso G, Broglia R, Muscari R. Investigation of asymmetrical shaft power increase during ship manoeuvres by means of model tests and CFD. In: Proc. of 29th symposium on naval hydrodynamics, Gotheborg; 2012.
- [4] Ribner H. NACA technical report, TR-820; 1943.
- [5] Atsavapranee P, Miller R, Day C, Klamo J, Fry D. Steady-turning experiments and RANS simulations on a surface combatant hull form (Model#5617). In: Proc. of 28th symposium on naval hydrodynamics, Pasadena, California; 2010.
- [6] Durante D, Broglia R, Muscari R, Di Mascio A. Numerical simulations of a turning circle manoeuvre for a fully appended hull. In: Proc. of 28th symposium on naval hydrodynamics, Pasadena, California; 2010.
- [7] Broglia R, Dubbioso G, Durante D, Di Mascio A. Simulation of turning circle by CFD: analysis of different propeller models and their effect on manoeuvring prediction. *Appl Ocean Res* 2013;39(1):1–10.
- [8] Broglia R, Dubbioso G, Di Mascio A. Prediction of manoeuvring properties for a tanker model by computational fluid dynamics. In: Specialist meeting on assessment of stability and control prediction methods for NATO air and sea vehicles (AVT-189), UK; 2011a.
- [9] Chang P, Elbert M, Young Y, Liu Z, Mahesh K, Jang H, et al. Propeller forces and structural response due to crashback. In: Proc. of 27th symposium on naval hydrodynamic, Seoul, Korea; 2008.
- [10] Pereira F, Salvatore F, Di Felice F, Soave M. Experimental investigation of a cavitating propeller in non-uniform inflow. In: Proc. of 25th symposium on naval hydrodynamic, St. John's, Newfoundland; 2004.
- [11] Salvatore F, Pereira F, Felli M, Calcagni D, Di Felice F. Description of the INSEAN E779A propeller experimental dataset. Tech. rep., Rapporto Tecnico INSEAN 206-085; 2006.
- [12] Muscari R, Felli M, Di Mascio A. Numerical and experimental analysis of the flow around a propeller behind a fully appended hull. In: Proc. of 28th symposium on naval hydrodynamics, Pasadena, California; 2010.
- [13] Carrica PM, Castro AM, Stern F. Self-propulsion computations using a speed controller and a discretized propeller with dynamic overset grids. *J Marine Sci Technol* 2010;15(4):316–30.
- [14] Carrica PM, Ismail F, Hyman M, Bhushan S, Stern F. Turn and zigzag manoeuvres of a surface combatant using a URANS approach with dynamic overset grids. In: Proc. SIMMAN 2008 workshop on verification and validation of ship manoeuvring simulation methods, Copenhagen, Denmark; 2008.
- [15] Carrica PM, Stern F. DES simulations of the KVLC1 in turn and zigzag manoeuvres with moving propeller and rudder. In: Proc. SIMMAN 2008 workshop on verification and validation of ship manoeuvring simulation methods, Copenhagen, Denmark; 2008.
- [16] Broglia R, Durante D, Dubbioso G, Di Mascio A. Turning ability characteristics study of a twin screw vessel by CFD. In: Marine 2011, Lisbon, Portugal, September 2011; 2011b.
- [17] Spalart PR, Allmaras SR. A one-equation turbulence model for aerodynamic flows. *La Recherche Aérospatiale* 1994;1:5–21.
- [18] Di Mascio A, Broglia R, Favini B. A second order Godunov-type scheme for naval hydrodynamics. Kluwer Academic/Plenum Publishers; 2001. 253–61.
- [19] Di Mascio A, Muscari R, Broglia R. An overlapping grids approach for moving bodies problems. In: Proc. of 16th int. offshore and polar engineering conference, San Francisco, California (USA); 2006.
- [20] Di Mascio A, Broglia R, Muscari R. On the application of the one-phase level set method for naval hydrodynamic flows. *Comput Fluids* 2007;36(5): 868–86.
- [21] Di Mascio A, Broglia R, Muscari R. Prediction of hydrodynamic coefficients of ship hulls by high-order Godunov-type methods. *J Marine Sci Technol* 2009;14:19–29.
- [22] Broglia R, Di Mascio A, Amati G. A parallel unsteady RANS code for the numerical simulations of free surface flows. In: Proc. of 2nd international conference on marine research and transportation, Ischia, Naples, Italy; 2007a.
- [23] Godunov SK. A finite difference method for the numerical computation of discontinuous solutions of the equations of fluid dynamics. *Mater Sb* 1959;47:271.
- [24] Harten A, Engquist B, Osher S, Chakravarthy SR. Uniformly high order accurate essentially non-oscillatory schemes. *J Comput Phys* 1987;71:231–303.
- [25] Van Leer B. A second-order sequel to Godunov's method Towards the ultimate conservative difference scheme V. *J Comput Phys* 1979;32:101–36.
- [26] Merkle CL, Athavale M. Time-accurate unsteady incompressible flow algorithm based on artificially compressibility. *AIAA paper 87-1137*; 1987.
- [27] Chorin A. A numerical method for solving incompressible viscous flow problems. *J Comput Phys* 1967;2:12–26.
- [28] Beam RM, Warming RF. An implicit factored scheme for the compressible Navier-Stokes equations. *AIAA J* 1978;16:393–402.
- [29] Favini B, Broglia R, Di Mascio A. Multi-grid acceleration of second order ENO schemes from low subsonic to high supersonic flows. *Int J Numer Methods Fluids* 1996;23:589–606.
- [30] Muscari R, Di Mascio A. Simulation of the flow around complex hull geometries by an overlapping grid approach. In: Proc. 5th Osaka Colloquium, Osaka, Japan; 2005.
- [31] Broglia R, Di Mascio A, Muscari R. Numerical study of confined water effects on a self-propelled submarine in steady manoeuvres. *Int J Offshore Polar Eng* 2007;17:89–96.
- [32] Muscari R, Felli M, Di Mascio A. Analysis of the flow past a fully appended hull with propellers by computational and experimental fluid dynamics. *J Fluid Eng* 2011;133:061104-1–061104-16.
- [33] Muscari R, Di Mascio A. Simulation of the viscous flow around a propeller using a dynamic overlapping grid approach. In: First international symposium on marine propulsors (SMP'09), Trondheim, Norway; 2009.
- [34] Muscari R, Di Mascio A. Numerical simulation of the flow past a rotating propeller behind a hull. In: Second international symposium on marine propulsors (SMP'11), Hamburg, Germany; 2011.
- [35] Leishmann JG, Beddoes TS. A semi-empirical model for dynamic stall. *J Am Helicopter Soc* 1989;34(3):3–17.
- [36] Leishmann J. Principles of helicopter aerodynamics. Wiley; 2006.
- [37] Coleman R, Feingold A, Stempin C. Evaluation of the induced velocity fields of an idealized helicopter rotor. NACA TR-29; 1945.
- [38] Roache PJ. Quantification of uncertainty in computational fluid dynamics. *Ann Rev Fluid Mech* 1997;29:123–60.
- [39] Gutshe F. The study of ships' propellers in oblique flow. Tech. rep., vol. 4306 DRIC translation, Defense Research Information Centre; 1975.
- [40] Phillips W, Anderson E, Kelly Q. Predicting the contribution of running propellers to aircraft stability derivatives. *J Aircraft* 2003;40(6):1107–14.